# Aperture masking imaging

Michael J. Ireland

**Abstract** Aperture-mask interferometry has a long history in the speckle regime - in principle equalling the performance of speckle interferometry in the low-flux, zero read-noise regime and offering superior calibration in the bright regime. Since adaptive optics has become commonplace on large telescopes, the key advantage of aperture-mask interferometry is in calibration, particularly of low spatial-frequency phase aberrations that cause quasi-static speckles. I will describe the principles of quasi-static speckle limited imaging in the Fourier plane, where bispectral phase (or Kernel-phase) and Fourier power are the primary observables, and will show that where Strehls are low or moderate, a non-redundant aperture can offer superior imaging performance. Finally, I will demonstrate the applicability of aperture-masking imaging both to laser-guide star imaging of faint ($K{\sim}14$) star systems and bright transition disk stars (e.g. LkCa 15) surrounded by faint (1000:1 dynamic range) structures..

**Key words:** aperture mask interferometry, sparse aperture masking, extrasolar planets, adaptive optics, optical interferometry

## 1 Introduction

The problem of achieving the full diffraction limit of a telescope through the use of aperture masking has a long history. Hippolyte Fizeau suggested in 1868 that this could be achieved through the use of a non-redundant (2-hole) aperture mask well before a modern understanding of the effects of astronomical seeing had been developed (Fizeau, 1868). When combined with the human eye as a fast detector,

Michael J. Ireland

Research School of Astronomy and Astrophysics
Australian National University, ACT 2611, Australia
e-mail: michael.ireland@anu.edu.au

such aperture masks, or later, an interferometer (Michelson and Pease, 1921), could be used to both resolve close binary stars and measure the sizes of stars.

In early eyepiece observing, the human brain was also an effective computer in recovering moderate contrast binary stars from speckle patterns at separations well below the seeing limit (Doolittle and Hough, 1907). In this case, a single speckle pattern is easily distinguished from two identical speckle patterns separated by more than the diffraction-limit but less than a seeing disk size if there is sufficient diversity in the observed speckle patterns, or if occasional "lucky" images show reduced Full-Width-Half-Maximum (FWHM) along the projected axis of the binary star. The dominance of the photographic plate in seeing-limited observations meant that after the decommissioning of the 20ft interferometer for the Mt Wilson 100 inch telescope, diffraction limited observing had a period of hiatus - only to be re-born with video-rate detection and optical Fourier transforms (Gezari et al., 1972).

Since the 1980s, electronic detectors and fast computers have enabled both a movement from 2-hole aperture masks to many-hole masks, and the exploitation of bispectral phase when speckle imaging with an unmasked pupil (Lohmann et al., 1983). These techniques have been limited both by detector noise at fast readout rates as well as low signal-to-noise in the many speckle regime. Some of the greatest imaging achievements from bispectrum speckle interferometry prior to regular adaptive optics observing remain unsurpassed. Full pupil speckle masking achieved dynamic ranges of $10^4$ (Weigelt et al., 2002) while non-redundant masking achieved precision calibration and reliable super-resolved imaging (Tuthill et al., 1999).

The decade from 2005 to 2015 has been characterised by adaptive optics imaging with low to moderate Strehl ratios, and infrared detectors with relatively high noise when short exposures are used, combined with limited data rates. This has meant that image analysis techniques for typical AO imaging have been often borrowed from space-based or seeing-limited observing. Aperture mask interferometry has played a key role in precision calibration of interferometric observables - visibility amplitudes and closure phases - that enable imaging and model fitting and image reconstruction at or beyond the formal diffraction limit.

The coming years offer further revolutions in imaging. Despite great advances in adaptive optics performance, limitations such as the cone effect in laser guide star adaptive optics and the need for very bright stars for extreme adaptive optics means that imaging will generally be done in the low to moderate Strehl ratio regime. In this regime, deconvolution or model fitting methods borrowed from spaced-based observing are flawed, and obtaining point-spread function references from wide field observing is only possible in crowded fields. However, low to moderate Strehl ratio imaging need not remain the same - for example, new low noise infrared detectors mean that speckle imaging behind adaptive optics will again be possible, providing a clear role for advanced diffraction-limited analysis techniques. Indeed, the move towards infrared (rather than visible) adaptive optics corrected laser guide star tip/tilt references mean that infrared data will begin to be routinely collected on stars bright enough for speckle techniques. However, as we will see in this chapter, optimising pupil geometry using a non-redundant aperture mask has clear calibra-

tion advantages in the low to moderate Strehl ratio regime, and it will continue to have a clear role 150 years after its birth.

In this chapter, I will attempt to put aperture masking imaging in a proper context by first outlining the general problem of narrow-field imaging in section 2, focusing on the difficulties in precision calibration. In section 3 I will describe the principles of aperture masking, focusing on the key observables of visibility amplitude and closure-phase, and will describe how closure-phase differs from kernel-phase and bispectral phase in section 4. Finally, I will show some examples of aperture mask imaging in section 5 and then conclude.

## 2 Narrow Field Imaging

In the case of generic narrow-field imaging, neglecting effects of polarisation, we consider the observed image $i(\boldsymbol{\alpha})$ of an object intensity distribution $o(\boldsymbol{\alpha})$ in the presence of a space-invariant Point-Spread Function (PSF) $m(\boldsymbol{\alpha})$, and can write:

$$i(\boldsymbol{\alpha}) = m(\boldsymbol{\alpha}) * o(\boldsymbol{\alpha}) \qquad (1)$$

Here, $\boldsymbol{\alpha}$ the 2-dimensional angular image vector in the image plane and $*$ represents convolution. In the Fourier domain, this is:

$$I(\boldsymbol{u}) = M(\boldsymbol{u}) \cdot O(\boldsymbol{u}) \qquad (2)$$

Here we have taken $I$ to be the 2-dimensional Fourier transform of $i$ (same for $m$ and $o$), and write the image spatial frequency vector as $u$. Multiplication in the Fourier domain is computationally simpler than convolution in the image domain, but is otherwise equivalent. As long as the recorded image $i$ is Nyquist-sampled, the *optical transfer function M* and therefore the image Fourier transform $I$ is bounded in the Fourier domain by the auto-correlation of the pupil.

At this point, in speckle imaging and aperture-mask interferometry, it is conventional to split into modulus and phase components:

$$|O(\boldsymbol{u})| = |I(\boldsymbol{u})|/|M(\boldsymbol{u})| \qquad (3)$$
$$\mathrm{Arg}[O(\boldsymbol{u})] = \mathrm{Arg}[I(\boldsymbol{u})] - \mathrm{Arg}[M(\boldsymbol{u})], \qquad (4)$$

with $|M|$ and $\mathrm{Arg}[M]$ e.g. estimated from observations of unresolved reference sources or reconstructed from a large number of observations of the bispectrum (Lohmann et al., 1983). Rather than going down this path, let us consider first the general problem of image reconstruction with both uncertainties in the data and with uncertain point-spread functions.

When presented with an image $i$, it is tempting to want to derive object properties directly from the image. For example, the use of aperture-photometry on an adaptive optics image where sources are well-resolved uses the approximation that

each aperture contains flux from only one object. This approximation breaks down in the presence of large PSF wings, or when objects are barely resolved. Where an image of a bright source dominates an image, it can be tempting to subtract the a model point-spread function from the image, and make inferences from the residual image. This kind of approach is not always possible or necessary, and rarely optimal. Instead, all we need to be able to do is to forward-model an object $o$ to see if it fits an image $i$. The inverse process can then be viewed as a detail - simply minimising chi-squared or maximising likelihood in the presence of a regulariser and prior knowledge using Bayesian techniques. Explicitly:

$$L(o|i) = L(i|o)P(o), \tag{5}$$

where $P(o)$ is the prior probability of a given object $o$. For readability, we will not write the prior probability $P(o)$ on the right hand side of the following equations, but note that it is often important to include, e.g. in the use of a maximum entropy regulariser.

The fundamental problem in determining if an object $o$ is consistent with an image $i$ is that the point-spread function $m$ is variable. Imagine being able to perfectly characterise $m$ experimentally by taking images of unresolved sources in all possible conditions. Then we could write:

$$L(o|i) = \int_m \exp(-\Sigma_j \frac{((m*o)_j - i_j)^2}{2\sigma_j^2})f(m), \tag{6}$$

where $i_j$ is now the image observed at pixel $j$, and the function $f(m)$ is the assumed known probability density function of PSFs $m$. Of course, in a more general case, we have a set of observed images $\{i_k\}$, in which case the likelihood function becomes a product over likelihoods for each image $k$:

$$L(o|\{i_k\}) = \Pi_k \int_m \exp(-\Sigma_j \frac{((m*o)_j - i_{k,j})^2}{2\sigma_{k,j}^2})f(m) \tag{7}$$

The only reason that more complex approaches than this (e.g. Fourier domain imaging) are used is that this is computationally difficult. For e.g. a 10 x 10 pixel arbitrary point-spread function, the integrals are integrals over 100 dimensions, almost certainly computed with Monte-Carlo techniques. The space of PSFs $m$ is also difficult to characterise - for the Hubble space telescope, all breathing modes could be parameterised by a few numbers, but e.g. speckle imaging in the presence of both random and static aberrations is more complex. It is important to realise, however, that moving beyond this equation is only done for reasons of computational simplicity, and not anything fundamentally *better* about Fourier, bispectral or kernel-phase techniques.

One simplification of the problem is to only consider the *high-Strehl* regime where the image is *dominated by diffraction of quasi-static speckles*. A *quasi-static speckle* is in our context seen as resulting from slowly varying pupil-plane phase

aberrations, which cause slowly varying image artefacts (speckles) in standard adaptive optics imaging. In this case, the diversity of images can be characterised by a mean $\bar{i}$ and a covariance matrix of the mean, taking into account the uncertainties due to PSF variation, which are added to the pixel-based uncertainties $\sigma_{j,k}$. This removes the product over all images $k$, leaving us with:

$$L(o|\{i\}) = \int_{\bar{m}} \exp(-\frac{1}{2}((\bar{m}*o)^k - \bar{i}^k)(C_k^j)^{-1}((\bar{m}*o)_j - \bar{i}_j))f(\bar{m}) \qquad (8)$$

Here $C_k^j$ is the covariance matrix derived from the set of images and the knowledge of pixel uncertainties, with an Einstein summation convention assumed. Although it is not in general possible to create an invertible sample covariance matrix directly from a small set of images, it is certainly possible once pixel variances are explicitly taken into account (which gives a diagonal approximation to $C_k^j$). As only the mean image $\bar{i}$ is explicitly considered, the PSF must also be considered as a mean over the number of exposures $\bar{m}$, and not a set of instantaneous PSFs. A move from here to the Fourier domain is not trivial, but is simplified by assuming that Fourier amplitude and phase are independent. We will write the amplitude as $\boldsymbol{O}_A$ , $\boldsymbol{M}_A$ and $\boldsymbol{I}_A$ - vectors of length equal to the number of sampled Fourier points, and will write the phase as $\boldsymbol{O}_\phi$, $\boldsymbol{M}_\phi$ and $\boldsymbol{I}_\phi$. For the amplitude, we have:

$$L(\boldsymbol{O}_A|\{\boldsymbol{I}_A\}) = \int_{\bar{\boldsymbol{M}}_A} \exp(-\frac{1}{2}((\bar{\boldsymbol{M}}_A \circ \boldsymbol{O}_A) - \bar{\boldsymbol{I}})^T \underline{C_{I,A}}^{-1}((\bar{\boldsymbol{M}}_A \circ \boldsymbol{O}_A) - \bar{\boldsymbol{I}}_A))f(\bar{\boldsymbol{M}}_A). \quad (9)$$

It is possible to change to this vector and matrix notation (following e.g. Martinache, 2010) from the subscripted notation of Equation 8 because the restriction of the object Fourier transform $\boldsymbol{O}$ to a pixel grid in Fourier space does not lose information so long as the image $i$ goes to zero at the edge of the observed field of view. The symbol $\circ$ represents element-wise multiplication. If we can finally approximate the components of $\boldsymbol{M}$ to have a large amplitude relative to their dispersion (again, as part of the high-Strehl regime), then marginalising over all possible values of $\boldsymbol{M}$ is equivalent to adding a "calibration error" to the data covariance:

$$L(\boldsymbol{O}|\{\boldsymbol{I}\}) = \exp(-\chi_A^2/2) \times \exp(-\chi_\phi^2/2) \qquad (10)$$

$$\chi_A^2 = ((\bar{\boldsymbol{M}}_A \circ \boldsymbol{O}_A) - \bar{\boldsymbol{I}}_A)^T (\underline{C_{A,I}} + \underline{C_{A,M}})^{-1}((\bar{\boldsymbol{M}}_A \circ \boldsymbol{O}_A) - \bar{\boldsymbol{I}}_A)) \qquad (11)$$

$$\chi_\phi^2 = (\bar{\boldsymbol{M}}_\phi - \bar{\boldsymbol{I}}_\phi - \boldsymbol{O}_\phi)^T (\underline{C_{I,\phi}} + \underline{C_{M,\phi}})^{-1}(\bar{\boldsymbol{M}}_\phi - \bar{\boldsymbol{I}}_\phi - \boldsymbol{O}_\phi) \qquad (12)$$

Even in the high-Strehl regime, this is not an especially simple process, as the large covariance matrices are in general highly non-diagonal in the presence of quasi-static speckle errors. The approach of the kernel-phase technique (Martinache, 2010; Ireland, 2013) is to ignore Fourier amplitudes and to project the Fourier phase uncertainties onto a subspace that is independent of pupil-plane phase errors to first order:

$$\underline{C_{I,\phi}} + \underline{C_{M,\phi}} = \underline{P}^T \mathrm{Diag}(\{\sigma^2\})\underline{P}. \qquad (13)$$

Here $\underline{P}$ is a projection matrix, and $\{\sigma^2\}$ are uncertainties on linear combinations of Fourier phases taken to be independent. We will discuss kernel-phase more in Section 4.

## 3 Non-Redundant Aperture Masking

In non-redundant aperture masking, a mask is placed in the pupil-plane of a telescope to enable more robust measurements of the object Fourier transform $O$. This robustness comes through two key avenues: higher amplitude of the optical transfer function $M_A$, especially at low Strehls, and a smaller dispersion in MTF amplitude and phase when influenced by phase errors (Ireland, 2013). The complexity to aperture-masking imaging comes in forming quantities that enable direct $\chi^2$ minimisation over possible object brightness distributions, independently of some distribution of PSFs (see Figure 1). One of these quantities is Fourier amplitude (as in Equation 3), also called visibility amplitude, especially when it applies to the object $|O|$ rather than the image. In order to made an unbiased estimator for amplitude at low signal-to-noise, the the squared visibility is typically used for fitting (Gordon and Buscher, 2012). The second key quantity is the closure-phase, also called bispectral phase.
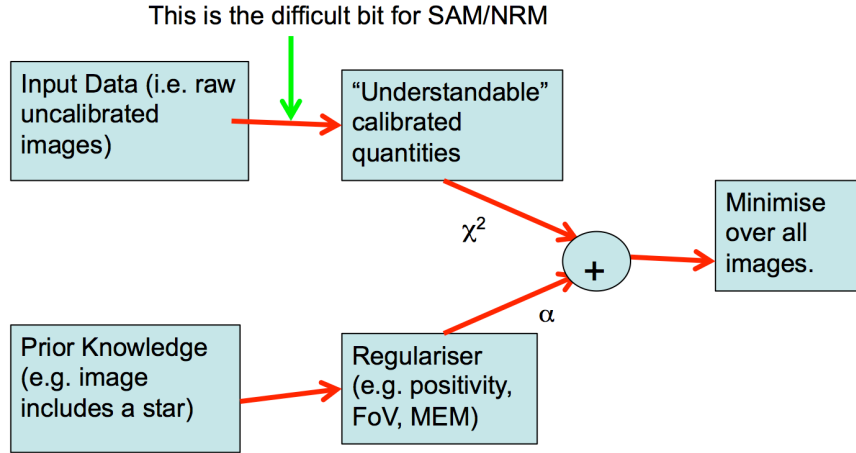


**Fig. 1** Generalised regularised imaging, showing schematically where the shift from raw pixel data to visibility amplitude and closure-phases occurs. The key difference to imaging with e.g. Equation 6 is that there is no marginalisation over all possible PSFs - the process of "calibration" is to form observables that relate directly to the target brightness distribution.

The closure phase is a quantity derived from the phase of three baselines that form a closing triangle in the telescope pupil. Figure 2 shows a single closing triangle. The bispectral point formed by these three complex Fourier amplitudes is given by their triple product, and the phase of this triple product is the closure phase. Once two baselines are defined, the third is given by the closure condition (two defined vectors give the reason for the *bi* in bispectrum). In two dimensional imaging, the bispectrum is therefore a 4-dimensional quantity. Where apertures are considered discrete, there can be a a much larger number of bispectrum vectors (closing triangles) than there are either baselines or apertures. The utility of the closure-phase is that a phase piston applied to any subaperture (caused by e.g. turbulence or thermal variations in an instrument) cancels in the closure phase, *so long as each Fourier point maps to a unique baseline in the pupil plane*. This is the property of *non-redundancy*.

For the simple non-redundant aperture mask shown in Figure 2, there are 4 closure-phases, of which only 3 are linearly independent:

$$\beta_1 = \phi_{AB} + \phi_{BC} + \phi_{CA} \tag{14}$$
$$\beta_2 = \phi_{AB} + \phi_{BD} + \phi_{DA} \tag{15}$$
$$\beta_3 = \phi_{AC} + \phi_{CD} + \phi_{DC} \tag{16}$$
$$\beta_4 = \phi_{BC} + \phi_{CD} + \phi_{DA} \tag{17}$$
$$= \beta_1 - \beta_2 + \beta_3 \tag{18}$$

The final line follows once the simple relationship $\phi_{AB} = -\phi_{BA}$ is appreciated. This follows directly from the well-known property of Fourier transforms of real functions (i.e. the image) being real - the Fourier transform is the complex conjugate of itself, rotated by 180 degrees. This means that for a 4-hole aperture mask, there are 3 linearly independent closure-phases, 4 closure-phases and 6 baselines. In general, for an $N_h$ hole *non-redundant* aperture mask, there are $N_b = N_h(N_h - 1)/2$ baselines, $N_{cp} = N_h(N_h - 1)(N_h - 2)/6$ closure-phases and $N_{ind} = (N_h - 1)(N_h - 2)/2 = N_b - N_h + 1$ linearly independent closure-phases.

Once squared Fourier amplitudes and closure-phases are formed for an image, the next step is to find appropriate calibrated quantities that refer to the true object brightness distribution. The averaged square amplitude of the MTF (i.e. the power spectrum) and the MTF bispectral phases are estimated from one or several point-spread function references. Following Equations 3 and 4, and neglecting the effects of photon bias which is discussed elsewhere (Gordon and Buscher, 2012), we have the following estimators for amplitude and bispectral phase:

$$\hat{O}_A^2 = \langle I_A^2 \rangle / \langle I_{A,\mathrm{Cal}}^2 \rangle \tag{19}$$
$$\hat{O}_\beta = \langle I_\beta \rangle - \langle I_{\beta,\mathrm{Cal}} \rangle \tag{20}$$
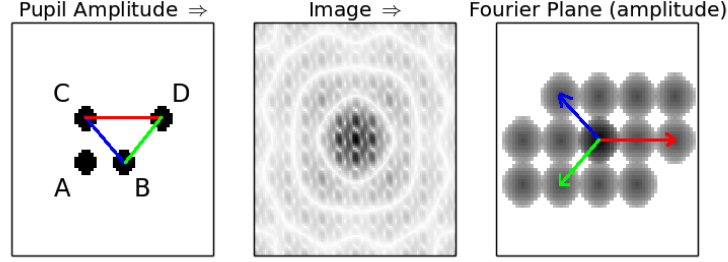
**Fig. 2** A 4-hole non-redundant aperture mask (left), the image formed by this in the case of no aberrations (centre) and the Fourier amplitude of the image (right). The Fourier transform of the image is the autocorrelation of the, pupil, meaning that baselines joining two points in the pupil plane correspond to vectors joining to origin to a $(u,v)$ point in the Fourier plane. If the pixel scale on the left is in $\Delta x$ metres, then the Fourier plane on the right has pixel units of spatial frequency in (dimensionless) units of $\Delta x/\lambda$, with $\lambda$ the observing wavelength.

Here the subscript "Cal" represents observations of a point-source calibrator, used to estimate the optical transfer function. Note that this calibration of phase by subtraction is generally applicable to any point-spread function (Equation 4), but the statement $\langle I_{\beta,\mathrm{Cal}} \rangle = 0$ is only approximately true in general in the presence of phase aberrations (Ireland, 2013). In order for easy model-fitting or image reconstruction of the object brightness distribution $o$ (i.e. Figure 1), for example using the first version of the OIFITS data format, these estimators are stored together with only the diagonal elements of their covariance matrices. Even neglecting photon bias, Equation 19 is in general a biased estimator for object square Fourier amplitude, with a relative uncertainty of order $\mathrm{SNR}_{\mathrm{Cal}}^{-2}$, where $\mathrm{SNR}_{\mathrm{Cal}}$ is the signal-to-noise ratio of the averaged calibrator square Fourier amplitudes. This is generally not taken into account, because typical observations have very high values of $\mathrm{SNR}_{\mathrm{Cal}}$, and because effects of non-Gaussian errors an incorrectly estimated covariance matrices for $\hat{O}_A^2$ are more significant effects. For aperture-masking observations behind adaptive optics, the effect of photon bias on the bispectrum is typically negligible, but not for the power spectrum.
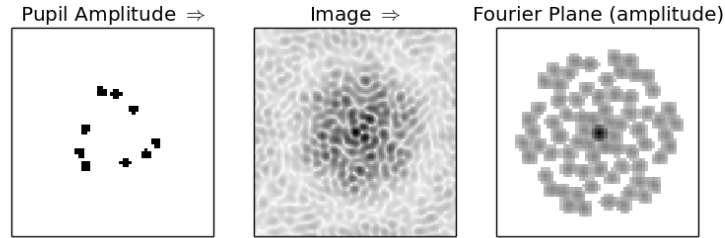


**Fig. 3** A 9-hole non-redundant aperture mask (left), the image formed by this in the case of moderate aberrations (centre), showing some asymmetry, and the Fourier amplitude of the image (right).
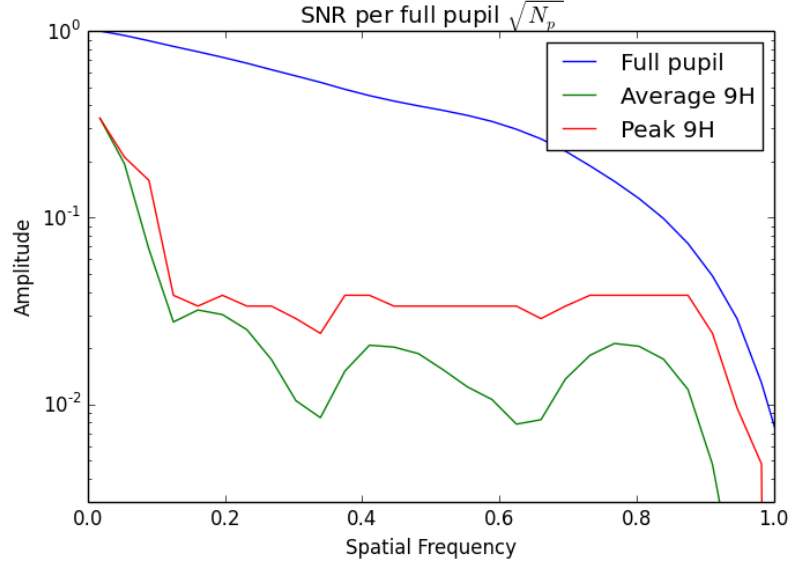
**Fig. 4** Fourier amplitude as measured in units of photons as a function of spatial frequency, scaled to a photon rate of 1 detected photon per unobstructed aperture. Three case are shown: an unobstructed pupil, the azimuthally averaged amplitude for observations of an unresolved object with a 9-hole non-redundant aperture mask, and the peak azimuthal amplitude for a 9-hole non-redundant aperture mask. As the 9-hole aperture-mask blocks most of the light, the amplitude significantly lower at zero spatial frequency (a measure of total object flux within the field of view), but is comparable to the unobstructed pupil for the highest spatial frequencies.

Now that we have considered the process of aperture-masking data calibration, let us consider and compare with the simpler process of imaging with an unobstructed aperture. Considering the data in the Fourier plane and neglecting PSF variations, this process amounts to measuring $\boldsymbol{O}_A$ and $\boldsymbol{O}_\phi$ for all pixels in the Fourier plane, and calibrating the Fourier data ready for image reconstruction or model fitting:

$$\hat{\boldsymbol{O}}_A = \langle \boldsymbol{I}_A \rangle / \langle \boldsymbol{I}_{A,\mathrm{Cal}} \rangle \tag{21}$$

$$\hat{\boldsymbol{O}}_\phi = \langle \boldsymbol{I}_\phi \rangle - \langle \boldsymbol{I}_{\phi,\mathrm{Cal}} \rangle \tag{22}$$

For a given incident flux rate, we can then ask how the photon shot noise limited signal to noise compares between non-redundant aperture masking and full pupil imaging. Figure 4 shows the result for the 9-hole aperture mask illustrated in Figure  - both techniques have comparable signal-to-noise for the longest baselines, but aperture masking loses significant signal to noise at short and intermediate baselines. The comparison is much less favourable for aperture masking if readout noise (or thermal noise from a warm mask) are significant. This demonstrates, as expected, that aperture masking should only be used when full pupil imaging is dominated

by calibration (e.g. quasi-static phase) errors, and if information contained in the longest baselines is essential for the science goal.

## 4 Kernel and Bispectral Phase

In recent years, the Fourier imaging techniques have been applied to redundant pupils geometries (such as an unobstructed pupil) in the case of adaptive optics imaging at moderately high Strehl ratios (Martinache, 2010). In kernel-phase imaging, the calibrated Fourier phase is viewed as a vector of phases at discrete locations (e.g. Equation 22), but all phase information is not used. The Fourier phase information is split into 2 subspaces, one that is independent to first order of pupil-plane aberrations, the kernel-phase, and one that can be used to determine the pupil-plane phase aberrations, which we will call the eigenphase (Martinache, 2013).

In aperture masking when considering sub apertures as point apertures, bispectral phases are closure-phases, and all closure-phases are independent of pupil-plane phase. Linear combinations of Fourier phases that are independent of pupil-plane phase are kernel-phases, so the terms *kernel-phase*, *closure phase* and *bispectral phase* can be used almost interchangeably. This is not the case for redundant pupil geometries - we will briefly consider the differences here.
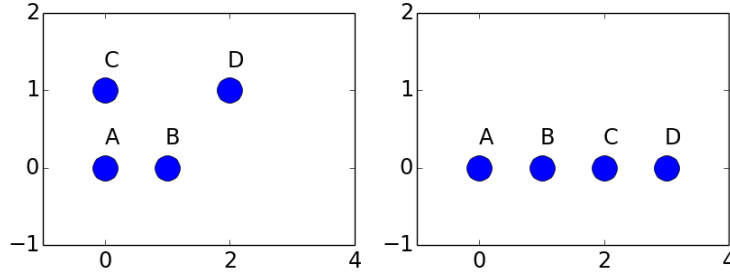


**Fig. 5** Left: A four-element non-redundant array with 3 kernel-phases and 3 independent bispectral phases. Right: A four-element redundant array with 1 kernel-phase and 2 independent bispectral phases.

In the example on the left of Figure 1, there are 4 sub-apertures, 6 baselines, 4 closure-phases and 3 statistically independent closure-phases or kernel-phases (discussed in Section 3). Consider the redundant example on the right in Figure 5, where we label phase for the baseline joining apertures A and B as $\phi_{AB}$. Due to redundancy, we have the identities:

$$\phi_{AB} = \phi_{BC} = \phi_{CD} \tag{23}$$

$$\phi_{AC} = \phi_{BD}, \tag{24}$$

Instead of 6 baselines, we only have 3, formed by the baselines between sub apertures A-B, A-C, and A-D. There are two bispectral phases, which are linearly independent of each other:

$$\beta_1 = \phi_{AB} + \phi_{BC} + \phi_{CA} \tag{25}$$

$$= 2\phi_{AB} - \phi_{AC} \tag{26}$$

$$\beta_2 = \phi_{AC} + \phi_{CD} + \phi_{DA} \tag{27}$$

$$= \phi_{AC} + \phi_{AB} - \phi_{AD} \tag{28}$$

However, neither of these are kernel-phases. As an example, imagine a 0.6 radian piston of aperture C. To compute the observed phase on baseline *AB*, we need to sum the complex fringe visibilities on the contributing baselines *AB*, *BC*, and *CD*. We can use small angle approximation, with $\mathrm{Arg}(\exp(i\phi_1) + \exp(i\phi_2)) \approx \phi_1 + \phi_2$, or simply sum complex visibilities. Either approach gives $\beta_1 = -0.3$ and $\beta_2 = +0.3$. The single kernel-phase in this example is formed from a linear combination of these bispectral phases:

$$\theta_1 = \beta_1 + \beta_2 \tag{29}$$

$$= 3\phi_{AB} - \phi_{AD} \tag{30}$$

This observable is robust to small phase errors - indeed, in a comparable way to closure-phases in non-redundant array example. For larger phase errors, the redundant array has a clear disadvantage. For example, imagine a $2\pi/3$ piston on sub-aperture *C*. This would produce fringes on baselines *AB*, *BC* and *CD* that would cancel when they are summed, producing no fringes and an indeterminate phase.

We can also apply the kernel-phase technique to highly redundant apertures, including for example non-redundant aperture masks if baselines *within* each sub aperture are included. The application of kernel-phase to a non-redundant mask and the Keck telescope pupil is shown in Figures 6 and 7. In this case, the pupil is represented by a square pixel grid. Although kernel-phases and eigen-phases are linear combinations of Fourier phases so can not be represented in the Fourier plane, we can project the Fourier phases onto the subspaces spanned by the set of eigen-phases and kernel-phases. It is this representation of phase that is illustrated in Figures 6 and 7. The peak to valley phase aberrations in this example are $\sim 2$ radians, which produces Strehl ratios of order 0.5 - the *moderate* Strehl ratio regime. In this regime, the redundant pupil geometry means that high Fourier amplitudes are retained for the case of the non-redundant mask, and kernel-phase remains robust to sub-aperture pistons.
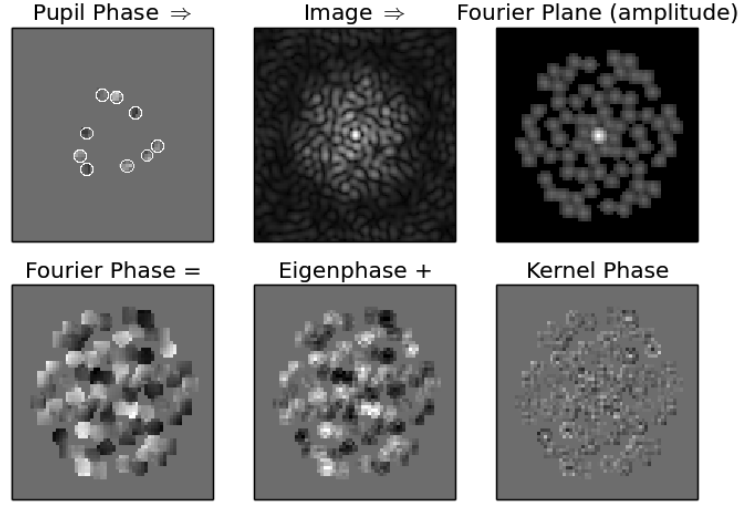
**Fig. 6** An illustration of splitting the information in the Fourier plane into amplitude, eigen-phase (Martinache, 2013) and kernel-phase (Martinache, 2010) for a 9-hole non-redundant aperture mask. Phase aberrations are dominated by pistons on each hole, which are not seen in the kernel-phase. The phase colour map corresponds to $\pm 1.25$ radians of phase, while the amplitude is shown in a cube-root stretch.

## 5 Applications of Aperture-Masking Imaging

Given the improved calibration to quasi-static speckle errors for aperture-masking imaging over imaging with an unobstructed pupil, there are a small number of key uses for the technique. It is clearly not the technique of choice when key observables are at moderate spatial frequency (e.g. objects resolved by several $\lambda/D$ that are faint enough to require long integrations). There are two key uses for aperture mask imaging that have emerged recently. Each of them applies only to observations where structures to be resolved are near the diffraction limit (e.g. a field of view less than about $4\lambda/D$, with $D$ the telescope diameter).

### 5.1 Precision Binary Astrometry

It is possible to measure accurate positions of stars in a partially resolved binary star system with aperture-masking, because the calibrated observables (Equations 19 and 20) relate directly to the object brightness distribution. There are numerous examples of this in the literature, for example Evans et al. (2012), where binary astrometry is possible down to separations of $\sim 0.5\lambda/D$. This is by no means a
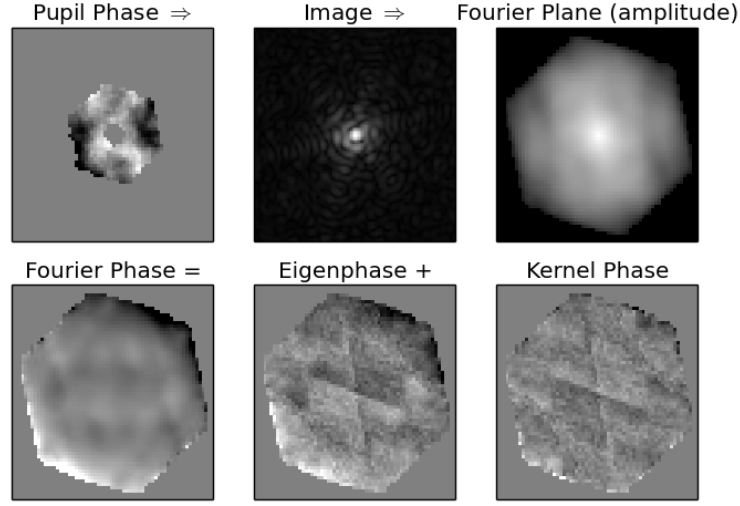
**Fig. 7** The same as Figure 6 but for an unobstructed pupil. The redundancy in the pupil means that aberrations can be clearly seen in the Fourier amplitude map, and Fourier phase does not separate as well into kernel-phase and eigenphase.

fundamental limitation, although contrast and separation become degenerate at the smallest separations, and require signal-to-noise inversely proportional to the cube of the separation. Unpublished orbits (e.g. Rizzuto et al 2015, in prep.) include astrometry down to $\sim 0.3 \lambda / D$.

## 5.2 Faint, Low-Strehl Imaging

Perhaps surprisingly, laser guide star observations of relatively faint object (down to K$\sim$15 with Keck) can be observed with higher fidelity using an aperture mask than with full pupil imaging. A recent example of this is Dupuy et al. (2015), where SDSS J105213.51+442255.7AB a binary brown dwarf with $K$ magnitudes of 15 and 15.5 was observed as part of an orbit monitoring program down to a separation of $\sim$30 milli-arcsec, with 1 milli-arcsec uncertainties. Due to the highly variable nature of laser guide star PSFs, these astrometric measurements would not have been possible without the use of the aperture mask. By searching over the space of all possible binary stars, data such as these are also useful for surveying for companions (e.g. Kraus et al. 2015, a survey of Kepler Objects of Interest, submitted), or imaging structures at the diffraction limit. Imaging complex, barely resolved structures is more difficult, because visibility amplitude calibrates very poorly, so only

point antisymmetric image components can be seen. Nonetheless, this is an exciting future prospect for aperture masking.

### 5.3 High-contrast Imaging (e.g. LkCa 15)

Aperture masking imaging has also been successfully used to detect faint structures and objects next to bright stars. Perhaps the most well known example of this is LkCa 15, a young star with a significant gas and dust depletion in the inner 20 AU of its disk (van der Marel et al., 2015), likely due to planetary formation. Aperture-masking imaging showed faint resolve structures, argued to be associated with planet formation (Kraus and Ireland, 2012). Subsequent observations of this system showed evidence for orbital motion (Ireland and Kraus, 2014) and also variability (e.g. compare Figure 8 to (Ireland, 2013)). One difficulty in interpreting these observations in general is that imaging based on closure-phases is not sensitive to point-symmetric structure, and both point-symmetric structure and barely-resolved flux close to the star is removed in an image regularisation process. As long as these issues are known, they can be robustly taken into account when interpreting aperture mask imaging (Cheetham et al., 2015)
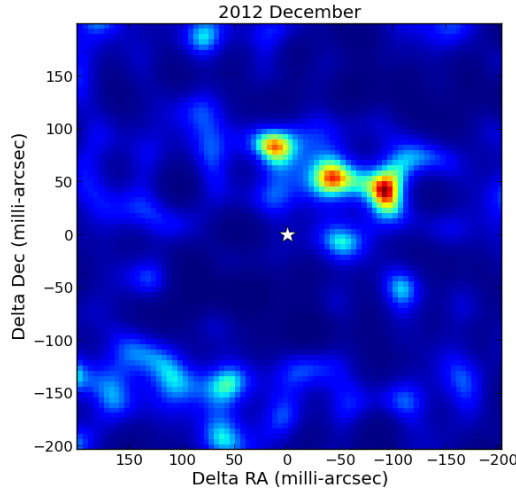


**Fig. 8** An example maximum entropy image reconstruction of LkCa 15, using the same data as presented in Ireland and Kraus (2014), and the algorithms as presented in Ireland (2013). As this is a fit to linear combinations of closure-phases only (i.e. kernel-phases), it is not sensitive to symmetric structures. The central point source is modelled separately from the image, an the brightest structures seen have a contrast of ∼250:1 from the central source.

# 6 Conclusions

The general problem of narrow-field imaging in astronomy is really a problem of reconstructing a model (or image) of an object brightness distribution from a noisy image in the presence of an only partially characterised PSF. This problem has a long history, and placing a mask with non-redundant sub aperture spacings over the pupil of a telescope is 150 years old. Through the use of an aperture-mask, the primary observables of closure-phase (or kernel-phase) and visibility amplitude can be accurately calibrated, enabling direct model fitting or image reconstruction based on these observables. Where Strehl ratios are high or targets are very faint, aperture masking may not be the best technique, but it excels at resolving and robustly calibrating structures right at the diffraction limit of a telescope. Given that adaptive optics is unlikely to deliver very high Strehl ratio images with high sky coverage in at least the next decade, aperture mask imaging will retain its role as the technique of choice for single-telescope diffraction limited imaging for some time to come.

# References

A. Cheetham, N. Huélamo, S. Lacour, I. de Gregorio-Monsalvo, P. Tuthill, Near-IR imaging of T Cha: evidence for scattered-light disc structures at Solar system scales. MNRAS **450**, 1–5 (2015). doi:10.1093/mnrasl/slv033

E. Doolittle, G.W. Hough, Catalogue and re-measurement of the 648 double stars discovered by Professor G.W. Hough. Publications of the University of Pennsylvania Flower Astronomical Observatory **3**, 1 (1907)

T.J. Dupuy, M.C. Liu, S.K. Leggett, M.J. Ireland, K. Chiu, D.A. Golimowski, The Mass-Luminosity Relation in the L/T Transition: Individual Dynamical Masses for the New J-band Flux Reversal Binary SDSSJ105213.51+442255.7AB. ApJ **805**, 56 (2015). doi:10.1088/0004-637X/805/1/56

T.M. Evans, M.J. Ireland, A.L. Kraus, F. Martinache, P. Stewart, P.G. Tuthill, S. Lacour, J.M. Carpenter, L.A. Hillenbrand, Mapping the Shores of the Brown Dwarf Desert. III. Young Moving Groups. ApJ **744**, 120 (2012). doi:10.1088/0004-637X/744/2/120

H. Fizeau, Prix bordin: Rapport sur le concours de l'anneé 1867. C.R.Acad.Sci. **66**, 932–934 (1868)

D.Y. Gezari, A. Labeyrie, R.V. Stachnik, Speckle Interferometry: Diffraction-Limited Measurements of Nine Stars with the 200-INCH Telescope. ApJ **173**, 1 (1972). doi:10.1086/180906

J.A. Gordon, D.F. Buscher, Detection noise bias and variance in the power spectrum and bispectrum in optical interferometry. A&A **541**, 46 (2012). doi:10.1051/0004-6361/201117335

M.J. Ireland, Phase errors in diffraction-limited imaging: contrast limits for sparse aperture masking. MNRAS **433**, 1718–1728 (2013). doi:10.1093/mnras/stt859

M.J. Ireland, A.L. Kraus, Orbital Motion and Multi-Wavelength Monitoring of LkCa15 b, in *IAU Symposium*, ed. by M. Booth, B.C. Matthews, J.R. Graham IAU Symposium, vol. 299, 2014, pp. 199–203. doi:10.1017/S1743921313008326

A.L. Kraus, M.J. Ireland, LkCa 15: A Young Exoplanet Caught at Formation? ApJ **745**, 5 (2012). doi:10.1088/0004-637X/745/1/5

A.W. Lohmann, G. Weigelt, B. Wirnitzer, Speckle masking in astronomy - Triple correlation theory and applications. Appl. Opt. **22**, 4028–4037 (1983)

F. Martinache, Kernel Phase in Fizeau Interferometry. ApJ **724**, 464–469 (2010). doi:10.1088/0004-637X/724/1/464

F. Martinache, The Asymmetric Pupil Fourier Wavefront Sensor. PASP **125**, 422–430 (2013). doi:10.1086/670670

A.A. Michelson, F.G. Pease, Measurement of the diameter of $/alpha$ orionis with the interferometer. ApJ **53**, 249 (1921)

P.G. Tuthill, J.D. Monnier, W.C. Danchi, A dusty pinwheel nebula around the massive star WR104. Nature **398**, 487–489 (1999). doi:10.1038/19033

N. van der Marel, E. van Dishoeck, S. Bruderer, L.M. Perez, A. Isella, Gas density drops inside dust cavities of transitional disks around young stars observed with ALMA. ArXiv e-prints (2015)

G. Weigelt, Y.Y. Balega, T. Preibisch, D. Schertl, M.D. Smith, Bispectrum speckle interferometry of the massive protostellar object S140 IRS 1: Evidence for multiple outflows. A&A **381**, 905–913 (2002). doi:10.1051/0004-6361:20011562